











High-Frequency Inductive Power Transfer Through Soil for Agricultural Applications

Juan M. Arteaga , John Sanchez, Faraj Elsakloul, Maria Marin, Cody Zesiger , Nunzio Pucci , *Member, IEEE*, Gareth J. Norton , Darrin J. Young , *Senior Member, IEEE*, David E. Boyle , *Member, IEEE*, Eric M. Yeatman , *Fellow, IEEE*, Paul D. Hallett , Shad Roundy , *Member, IEEE*, and Paul D. Mitcheson , *Senior Member, IEEE*

Abstract—This article presents 13.56-MHz inductive power transfer (IPT) through soil for sensors in agricultural applications. Two IPT system designs and their prototypes are presented. The first was designed for gathering data and observing the relationship between the performance of the coil driving circuits in response to water content, salinity, organic matter, and compaction of the soil. The second prototype was designed as an application demonstrator, featuring IPT to an in-house sensor node enclosure buried 200 mm under the surface of an agricultural field. The results highlight that from the parameters studied, the combination of high salinity and high water content significantly increases the losses of the IPT system. The experiments demonstrate an over 40% rise in the losses from dc source to dc load after a 16% increase in soil water content and high salinity. In the technology demonstrator, we mounted an IPT transmitter on a drone to wirelessly power an in-house bank of supercapacitors in the buried sensor-node enclosure. A peak power transfer of 30 W received at over 40% efficiency was achieved from a 22-V power supply on the drone to the energy storage under the ground. The coil separation in these experiments was 250 mm of which 200 mm correspond to the layer of soil. The coupling factor in all the experiments was lower than 5%. This system was

tried in the field for 40 days and wireless power was performed 5 times throughout.

Index Terms—Electromagnetic measurements, smart agriculture, wireless power transmission.

I. INTRODUCTION

INDUCTIVE power transfer (IPT) has been rolled out in consumer applications [1] and has been demonstrated and trialed for wireless charging of electric vehicles [2], [3]. There are applications where wireless charging is crucial, for example, in medical implants [4], [5], [6], [7] and emerging autonomous systems [8], [9], [10]. In agricultural applications, the inclusion of wireless power transfer could be transformational, as it unlocks a nondisruptive means to charge sensors buried in soil, which are critical for automation and optimization [11], [12].

Commercially available IPT systems can achieve high efficiency (>80%) with wireless gaps smaller than a few centimeters [1]. This limits the range of applications, excluding those that require large wireless gaps and spatial freedom. The separation between the transmitter and the receiver in IPT is largely dictated by the size of the coils (the gap is usually normalized to the coils' radius or diameter), [13], [14] and the Q -factor. Unfortunately, scaling up existing commercially available IPT coils, which are typically designed to be driven at frequencies lower than 200 kHz, is not straightforward or practical due to the complexity of the coils, which tend to employ ferrites for flux shaping and shielding and a considerable number of turns of litz wire. At megahertz, high- Q can be achieved with relatively simple air-core coils from printed circuit board (PCB) traces, copper pipe, or solid wire, typically with one to five turns [15], [16], [17], [18], [19]. However, designing and building the power electronics circuits to drive the coils at megahertz can be challenging [20]. An alternative to IPT is capacitive power transfer, where the capacitance between two pairs of plates conforms to a wireless link. This technology is well suited for a number of applications [21], and recent work has introduced new techniques to operate it in the presence of soil [22], [23]. Nonetheless, the application proposed in this work requires a small cross-sectional area, especially on the transmitter, relatively high power and large distance, which are challenges best addressed with IPT.

This work focuses on two high-frequency IPT (HF-IPT) system designs featuring 13.56-MHz power converters, where

Manuscript received 19 March 2023; revised 1 July 2023; accepted 5 August 2023. Date of publication 16 August 2023; date of current version 22 September 2023. This work was supported in part by the U.K. Research and Innovation (UKRI) under Grants NE/T011467/1 and NE/T011068/1, and in part by the National Science Foundation (NSF) under Grant 1935632: SitS NSF-UKRI: Wireless In-Situ Soil Sensing Network for Future Sustainable Agriculture. The work of Faraj Elsakloul was supported by the Libyan Embassy. Recommended for publication by Associate Editor Grant Anthony Covic. (*Corresponding author: Juan M. Arteaga.*)

Juan M. Arteaga is with the NewOrbit Space, Ltd., RG4 5AF Reading, U.K. (e-mail: juan@neworbit.space).

John Sanchez and Shad Roundy are with the Department of Mechanical Engineering, The University of Utah, Salt Lake City, UT 84112 USA (e-mail: u1319828@utah.edu; shad.roundy@utah.edu).

Faraj Elsakloul, Maria Marin, Gareth J. Norton, and Paul D. Hallett are with the School of Biological Sciences, University of Aberdeen, AB24 3FX Aberdeen, U.K. (e-mail: f.elsakloul.21@abdn.ac.uk; maria.marin@abdn.ac.uk; g.norton@abdn.ac.uk; paul.hallett@abdn.ac.uk).

Cody Zesiger is with the Agriculture and Natural Resources, Utah State University, Logan, UT 84322 USA (e-mail: cody.zesiger@usu.edu).

Nunzio Pucci, Eric M. Yeatman, and Paul D. Mitcheson are with the Department of Electrical and Electronic Engineering, Imperial College London, SW7 2BX London, U.K. (e-mail: nunzio.pucci15@imperial.ac.uk; e.yeatman@imperial.ac.uk; paul.mitcheson@imperial.ac.uk).

Darrin J. Young is with the Electrical and Computer Engineering Department, The University of Utah, Salt Lake City, UT 84112 USA (e-mail: darrin.young@utah.edu).

David E. Boyle is with the Dyson School of Design Engineering, Imperial College London, SW7 2BX London, U.K. (e-mail: david.boyle@imperial.ac.uk).

Color versions of one or more figures in this article are available at <https://doi.org/10.1109/TPEL.2023.3305642>.

Digital Object Identifier 10.1109/TPEL.2023.3305642

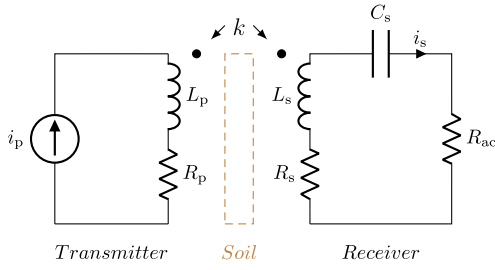


Fig. 1. Equivalent circuit of an IPT link through the soil.

wireless power is achieved not only with gaps larger than 200 mm but with soil between the coils. Soils can be modeled as nonferromagnetic dielectrics with variable magnetic permeability, real permittivity, and effective conductivity [24], [25]. These variable parameters would determine the performance of an HF-IPT link through the soil. Practically, for agricultural applications, major properties that may affect an HF-IPT link are water content, salinity, organic matter, and compaction, due to their impacts on dielectric permittivity. In the experiments, the effects from the soil in the performance of a 13.56-MHz IPT system are studied, first by testing a dc–dc wireless power transfer system with 19 samples of soil (with different parameters, representative to those in agricultural fields) between the coils, and finally, with a field trial featuring wireless power to an in-house sensor node, where an in-house bank of supercapacitors was charged. The receive coil was buried 200 mm under the surface of an agricultural field, and the tolerance to misalignment of the transmit coil at the surface in this experiment is 100 mm.

The rest of the article is organized as follows. Section II covers the theoretical background on the principles of IPT and introduces the Class EF inverter. Section III summarizes the state of the art on the estimation of inductively coupled resistances and reactances with Class EF inverters. Section IV describes HF-IPT experiments with samples of soil with different compositions. Section V proposes and showcases a practical demonstrator of the technology. Finally, Section VI concludes this article.

This article expands our previous works published as conference proceedings [26], [27].

II. BACKGROUND

A. Reflected Impedance of the Receivers and the Medium in IPT

An IPT link can be modeled as illustrated in Fig. 1. The inverter is represented by a current source (i_p) driving the transmit coil (L_p with an equivalent series resistor of R_p). The receiver is modeled as the receiver coil (L_s with an equivalent series resistor of R_s), a series capacitor (C_s) to resonate the receiver coil, and R_{ac} , representing an ac load or the input resistance of the rectifier. The circuit diagram in Fig. 1 illustrates the sample of soil which may affect how the two sides of the system interact: It may reflect a reactance to the inductively coupled coils detuning the resonant circuits, and it may produce heat, thus reflecting a resistance on the inductively coupled coils.

To model how the receiver loads the inverter and how the soil might detune the link or consume power, the equivalent circuit

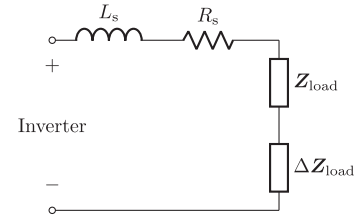


Fig. 2. Equivalent circuit of an IPT transmit coil with the reflected impedance from the load and its variation caused by the soil sample.

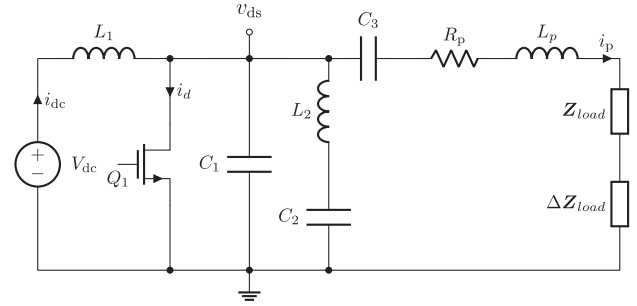


Fig. 3. Circuit diagram of the Class EF inverter with the inductively coupled load modeled as the sum of the impedances Z_{load} and ΔZ_{load} .

of the transmit coil with two inductively coupled reflected loads can be derived as illustrated in Fig. 2. This representation is useful for normalizing the operation of an inverter with the legitimate receiver (and no soil sample) and attributing any differences in the reflected impedance to the sample of soil. It should be noted that in this representation, ΔZ_{load} ¹ models not only the impedance reflected by the soil to the transmitter but also the changes produced on the receiver (e.g., detuning), which consequently change the impedance reflected by the receiver on the transmitter.

B. Class EF Inverter

The Class EF (see Fig. 3) is a single-switch resonant inverter. Its operating principle is similar to that of the Class E [28] but with the addition of the resonant branch (L_2 , C_2 in Fig. 3), which is tuned at a frequency higher than that driving the switch [29], [30], [31].

The design of the inverters in this work follows the load-independent concept introduced in [32] and was performed with the iterative procedure introduced in [33]. The load-independent design allows for the load to vary from zero ($\Delta Z_{load} = -Z_{load}$, in Fig. 3, i.e., no coupled circuit to the transmitter) to full load ($Z_{load} + \Delta Z_{load} = R_{load,max}$, in Fig. 3, in practice, a coupled circuit, which reflects a resistance that produces a loaded Q factor of roughly 10 [34] in the load branch), without affecting the amplitude and phase of the current in the coil. In addition, the trajectory of v_{ds} is locked to zero at turn-ON for any load within the range. Moreover, zero-voltage switching is achieved and conduction of the antiparallel diode of the switch is prevented for the entirety of the operating range. These features do not

¹Complex phasor quantities are marked as bold.

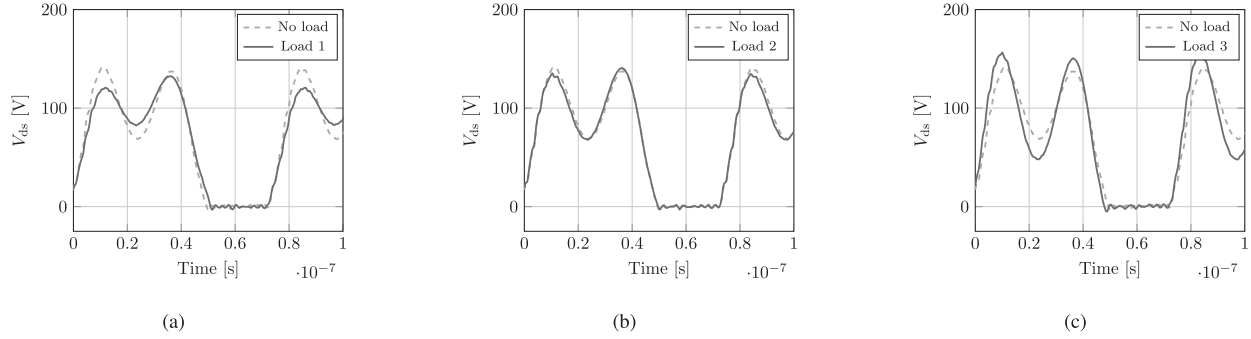


Fig. 4. Experimental waveforms of the drain–source voltage of the transistor of a Class EF inverter powering three inductively coupled known test loads. The waveforms from the unloaded inverter ($Z_{\text{load}} + \Delta Z_{\text{load}} = 0$; No Load) are shown as a reference. (a) Load 1: $Z_{\text{load}} + \Delta Z_{\text{load}} = 1.9 + 1.23j$. (b) Load 2: $Z_{\text{load}} + \Delta Z_{\text{load}} = 1.45 - 0.4j$. (c) Load 3: $Z_{\text{load}} + \Delta Z_{\text{load}} = 0.47 - 2.45j$.

hold when a reactance is reflected due to the detuning of the load network.

III. ESTIMATING THE IMPEDANCE OF AN INDUCTIVELY COUPLED LOAD FROM THE DRAIN VOLTAGE WAVEFORMS OF A CLASS EF INVERTER

Measuring the induced voltage from a load and the medium on an IPT transmit coil might seem straightforward from readings from the voltage across and the current through the coil. However, in practice, reliable attainment of these variables can be difficult or unreliable due to the parasitic capacitance of introducing a voltage probe across the coil (especially in this case where the coil is series-tuned), and the dependence of an accurate phase difference reading from the current and the voltage probes at megahertz frequencies.

To overcome these issues in HF-IPT with Class EF inverters, in [34], we proposed a technique where the phase and magnitude of the inductively coupled receiver (i.e., the total reflected resistance and the reflected reactance) are extracted in real time from v_{ds} using a mathematical model. It was demonstrated that the trajectory of v_{ds} has a direct correlation with the reflected impedance, and it can be obtained with good accuracy: A normalized root-mean-square error of 1.1% for the reflected resistance and 1.2% for the reflected reactance was achieved with the model proposed in [34]. Furthermore, in [35], it was demonstrated that the magnitude and phase of the load can be extracted solely from the input dc current and the magnitude of the first harmonic of the switching waveform with a similar accuracy: a root-mean-square error of 1% for the real part and 1.5% for the imaginary part [35].

The load-dependent shape of v_{ds} is illustrated in the plots in Fig. 4. These plots exemplify the changes in the trajectory of the drain-to-source voltage waveform of a Class EF inverter with different inductively coupled loads reflecting different resistances and reactances on the transmitter. The design of the inverter, the experimental setup, and the methodology from which these waveforms were obtained are discussed in Section IV.

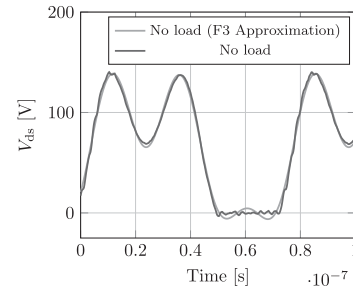


Fig. 5. Third-order Fourier series approximation of the experimental waveforms of the drain–source voltage of the transistor of a Class EF with respect to the experimental waveform.

A. Methodology and Example of the Formulation of the Reflected Impedance Model From Experimental Waveforms

In order to demonstrate the technique, we extract the amplitude and phase of the first three harmonics (which are the only ones with an amplitude higher than 1% of the input voltage) from the waveforms in Fig. 4 by fitting the data to a third-order Fourier series

$$v_{\text{ds}}(t)|_{F_3} = V_{\text{ds}} + a_1 \cos(\omega t) + b_1 \sin(\omega t) + a_2 \cos(2\omega t) + b_2 \sin(2\omega t) + a_3 \cos(3\omega t) + b_3 \sin(3\omega t). \quad (1)$$

The results from this approximation are exemplified for the case of no coupled load in Fig. 5, and the waveforms resulting from this approximation for the test loads are illustrated in Fig. 6.

From (1), we can quantify the magnitude and the relative phase of each of the harmonics and define them as

$$H_n = \sqrt{a_n^2 + b_n^2} \quad (2)$$

and

$$\Phi_n = \arctan \frac{b_n}{a_n} \quad (3)$$

with n being the harmonic under study. Table I summarizes the amplitude and phase of the first three harmonics of the Fourier-fitted waveforms, against each load, in addition to the measured

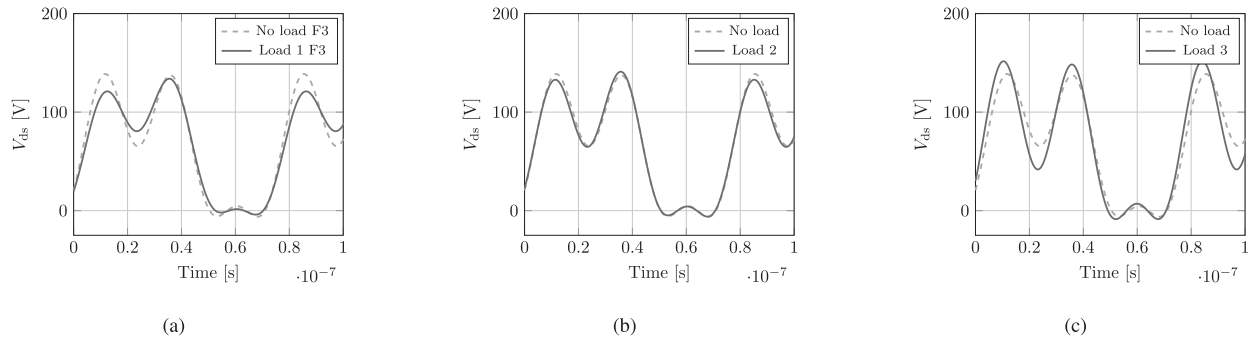


Fig. 6. Third-order Fourier series approximation of the experimental waveforms of the drain–source voltage of the transistor of a Class EF inverter powering three inductively coupled known test loads. The waveforms from the unloaded inverter (no load) are shown as a reference. (a) Load 1: $1.9 + 1.23j$. (b) Load 2: $1.45 - 0.4j$. (c) Load 3: $0.47 - 2.45j$.

TABLE I
SUMMARY OF THE DATA GATHERED IN THE IPT EXPERIMENTS WITH KNOWN LOADS

	Reflected load (Ω)	I_{dc} (A)	H_1 (V)	H_2 (V)	H_3 (V)	Φ_1	Φ_2	Φ_3	$ i_p $ (A)
No load	$0 + 0j$	0.11	61.8	27.1	31.4	16°	-13°	3°	3.86
Load 1	$1.9 + 1.23j$	0.27	63.1	20.8	23.2	15°	-12°	2°	3.63
Load 2	$1.45 - 0.4j$	0.25	61.1	27.4	30.8	15°	-12°	3°	3.85
Load 3	$0.47 - 2.45j$	0.14	57.5	37.7	40.1	17°	-12°	5°	4.12

input dc current (I_{dc}), and the amplitude of the current in the transmit coil (i_p).

From the data in Table I, it can be verified that as in [35], the most distinctive single variable to estimate the real component of the load is I_{dc} , and the most distinctive variables to estimate the imaginary part of the load are the amplitude of any of the first three harmonics of v_{ds} . As proposed in [35], we used a single variable first-order linear model to estimate each of the components of the load.

The linear model that estimates the real portion of the load is formulated as

$$R_{eq} = 10.9I_{dc} - 1.15 \quad (4)$$

and the model that estimates the imaginary portion of the load is formulated as

$$X_{eq} = 0.63H_1 - 38.62 \quad (5)$$

where H_1 is calculated from (2), with $n = 1$, from experimental waveforms or in real-time using a narrow-band filter as was shown in [36]. This model estimates the known loads (open circuit, Load 1, Load 2, and Load 3) within a 0.25- Ω range for each of the real and imaginary portions of the loads.

IV. HF-IPT THROUGH SAMPLES OF SOIL WITH CONTROLLED PARAMETERS

The reflected impedance estimation model formulated in Section III was used to monitor how soil samples between two coils performing HF-IPT affect the tuning and efficiency of the link. The experiments were designed to measure the power that is transferred from the dc source to the dc load and the impedance

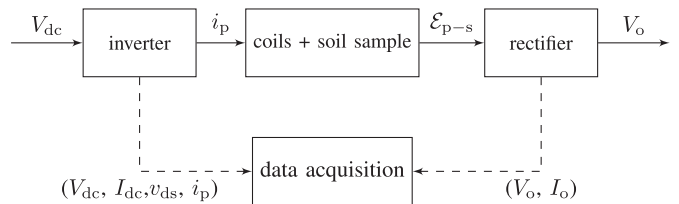


Fig. 7. Block diagram of the experimental setup design.

that is reflected to the transmitter from the combination of the receiver and the soil sample.

A. Experimental Setup Design

The experimental setup was designed as illustrated in the block diagram in Fig. 7. The recorded data were the input dc voltage (V_{dc}) and the input dc current (I_{dc}) from the power supply, the waveforms v_{ds} and i_p using a Lecroy 6104 A oscilloscope with a PHV 1000 voltage probe by PMK and a Keysight N2783B current probe, the output dc voltage (V_o) using a multimeter, and the output dc current (I_o) was calculated from V_o and the load resistance.

The transmitter and the receiver were designed to be enclosed in two equal plastic cases with the following internal dimensions: length: 370 mm, width: 270 mm, height: 150 mm. The transmit coil was mounted parallel to the lid of the box on top with a 5-mm air clearance. The receiver was mounted parallel to the bottom face of its enclosure with a 20-mm clearance (which is the minimum clearance at the bottom). The placement of the coils was selected for them to be as close as possible to the soil sample in between with the chosen enclosures.

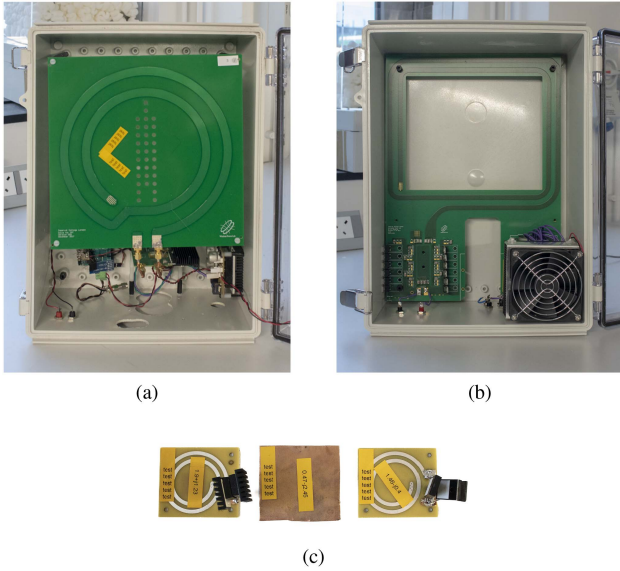


Fig. 8. Photographs of the circuit enclosures for the experiments with samples of soil. (a) Transmitter. (b) Receiver. (c) Calibration loads.

B. Design of the HF-IPT Transmitter and Receiver

A photograph of the enclosures with the transmitter and the receiver assembled for the experiments is shown in Fig. 8(a) and (b). The transmitter uses a 13.56-MHz Class EF inverter and a 2-turn 200-mm diameter coil (Fig. 8(a); a detailed design of this coil can be found in [37]). The inverter was mounted perpendicular to the coil for easier access to probe. The receiver was designed with the coil and the rectifier in a single printed circuit board [see Fig. 8(b)], with a voltage tripler rectifier. A test resistive dc load, ranging from 0 to 1000 Ω with ten 100- Ω steps and a maximum power of 200 W was included in the enclosure with plugs outside the enclosure to select the dc load and alter it during the experiments.

The inverter was designed to be load-independent (from [32, Table II], with $p = 3$, and $q_1 = 1.66$) with an input-voltage-to-output-current gain of $63 \text{ mA} \cdot \text{V}^{-1}$, and a maximum load of 5 Ω . From the simulation, the efficiency of the inverter can be slightly higher than 95% (without including the losses in the coil at maximum load, and previous work reported efficiencies of up to 83% with this design [17], from dc-source to dc-load. This inverter design has been evaluated in [34] for a wide range of loads including those not fully tuned, demonstrating the capabilities of operating well under slight detuning. The component values and properties, including the HF-IPT coil, are specified as Design 1 in Table II. The duty cycle of the transistor was set at 30%. The input voltage was set at 61.8 V in all the experiments.

Three test-loads [see Fig. 8(c)] were assembled to reflect three known loads to the transmit coil: one predominantly resistive, one predominantly inductive, and another resistive-capacitive. The reflected impedance of these test loads when placed in the allocated position [marked at the center of the coil in Fig. 8(a)] are as follows: Load 1 reflects $1.9 + 1.23j$, Load 2 reflects $1.45 - 0.4j$, and Load 3 reflects $0.47 - 2.45j$. The

TABLE II
COMPONENTS FOR THE INVERTERS

Component	Design 1	Design 2	Description
C_1 (pF)	$100 + C_{\text{OSS}}$	$110 + C_{\text{OSS}}$	TDK C Series
C_2 (pF)	200	200	TDK C Series
C_3 (pF)	144	144	EPCOS - TDK
L_2 (nH)	251	251	Coilcraft 2014VS
L_p (μH)	1.18	1.18	PCB or copper-pipe
Q_1	GS66504B (650 V, 15 A) GaN FET		

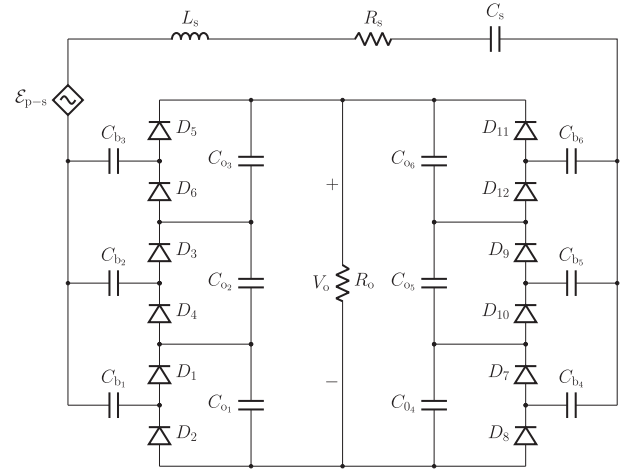


Fig. 9. Circuit diagram of a voltage-tripler full-wave Class D rectifier.

TABLE III
COMPONENTS FOR THE RECTIFIERS

Component	Design 1	Description
C_s (pF)	58.5	TDK C Series
$C_{o1} - C_{o6}, C_{b1} - C_{b6}$ (nF)	200	TDK C Series
L_s (nH)	2470	PCB coil
R_s (m Ω)	372	PCB coil
$D_1 - D_{12}$	Vishay MBRF10100 (100 V, 10 A) Schottky	

drain-source voltage waveforms of the inverter powering these loads are presented in Fig. 4.

The receiver implements a rectangular two-turn PCB coil (with external dimensions of 250 mm \times 200 mm, dictated by the dimension restrictions of the enclosure. The topology of the rectifier is the voltage tripler [38] Class D (see Fig. 9), which maximizes the induced-voltage-to-output-voltage gain of the rectifier (see Fig. 7), thus making changes in the link more easy to detect. The component values and properties of the rectifier are specified in Table III.

The coils and the reflected impedance from the calibration loads were measured with a Keysight E4990A impedance analyzer.

C. Preparation of the Soil Samples

The soil samples were obtained from SRUC Craibstone, Aberdeen, U.K. ($57^\circ 11' 13.3''$ N, $2^\circ 12' 49.6''$ W). It had a sandy

loam texture and was taken from a field under a ley-arable rotation. The soil was partially air-dried, mixed, and passed through a 4-mm sieve. The soil samples were packed in non-conductive containers with the following dimensions: length: 400 mm, width: 600 mm, height: 180 mm, and the soil was packed up to 100 mm in height. The soil dielectric constant was measured with a laboratory TDR Probe (E-Test TDR devices, Lublin, Poland). Water content was measured after each test by oven drying a subsampled soil core at 105 °C until water loss ceased. The samples were treated to produce different soil conditions specified in the following.

1) *Soil Water Content*: The soil was packed at approximately $1.1\text{-g} \cdot \text{cm}^{-3}$ bulk density and four levels of water content as follows: $0.16\text{-g} \cdot \text{g}^{-1}$, $0.26\text{-g} \cdot \text{g}^{-1}$, $0.35\text{-g} \cdot \text{g}^{-1}$, and $0.50\text{-g} \cdot \text{g}^{-1}$ water content.

2) *Soil Salinity*: Soil was packed in the containers at $1.1\text{-g} \cdot \text{cm}^{-3}$ bulk density and $0.2\text{-g} \cdot \text{g}^{-1}$ water content. Five salinity levels were implemented by adding NaCl at the following levels: $0\text{ g} \cdot \text{kg}^{-1}$, $0.3\text{ g} \cdot \text{kg}^{-1}$, $1.1\text{ g} \cdot \text{kg}^{-1}$, $4.4\text{ g} \cdot \text{kg}^{-1}$, and $28.2\text{ g} \cdot \text{kg}^{-1}$. In soil pore water, an average increment of $1\text{ dS} \cdot \text{m}^{-1}$ is obtained with the addition of 640 mg of NaCl.

3) *Soil Organic Matter Content*: The sieved soil was mixed with five concentrations of compost (passed through a 4-mm sieve): 0%, 5%, 10%, 20%, 30%. The amended soils were packed in the containers at $0.20\text{-g} \cdot \text{g}^{-1}$ water content and $1.1\text{-g} \cdot \text{cm}^{-3}$ bulk density.

4) *Soil Compaction*: Soil was packed in the containers at $0.20\text{-g} \cdot \text{g}^{-1}$ water content and five levels of bulk density: loose soil (approximately $0.9\text{ g} \cdot \text{cm}^{-3}$), gentle weight applied ($1.0\text{ g} \cdot \text{cm}^{-3}$), heavy weight applied ($1.1\text{ g} \cdot \text{cm}^{-3}$, and $1.3\text{ g} \cdot \text{cm}^{-3}$), and highly compacted ($1.5\text{ g} \cdot \text{cm}^{-3}$) using a proctor hammer. Table IV provides various properties of the soil samples.

D. Description of the Experiments

Three types of experiments were conducted. First, the transmit coil (without the inverter) was placed on top of each soil sample with an air gap of 10 mm between the coil and the soil. The equivalent impedance of the coil was measured in the presence of the sample with an impedance analyzer to verify that none of the samples would overload the transmitter. Second, the transmitter was placed facing the soil sample and switched on to verify the expected operation of the inverter in all cases. Finally, both ends of the system were placed with a soil sample between the coils as shown in the diagram in Fig. 10 to record the measurements.

Power was transferred through the inductive link, first in the presence of an empty enclosure and then with each of the nineteen soil samples. The dc load at the receiver side was stepped at $100\ \Omega$, $500\ \Omega$, and $1\text{ k}\Omega$ for each case. Measurements were also taken without the presence of the receiver to assess the reflection of the soil sample on its own to the transmitter.

After these experiments, water was added in real time to two samples with high salinity ($28.2\text{ g} \cdot \text{kg}^{-1}$ and $4.4\text{ g} \cdot \text{kg}^{-1}$), in order to observe the changes of the reflected impedance in real time, combining the two variables of water content and salinity, and without having to reposition the enclosures.

TABLE IV
SOIL TREATMENTS TESTED, INCLUDING MEASURED DIELECTRIC CONSTANT AND VOLUMETRIC WATER CONTENTS

Soil Treatment	Target	Dielectric Constant	Actual Water Content [$\text{m}^3 \cdot \text{m}^{-3}$]
Water Content	$0.16\text{ g} \cdot \text{g}^{-1}$	8.18	0.17
	$0.22\text{ g} \cdot \text{g}^{-1}$	10.31	0.23
	$0.35\text{ g} \cdot \text{g}^{-1}$	20.77	0.37
	$0.50\text{ g} \cdot \text{g}^{-1}$	33.05	0.63
Salinity (NaCl)	$0\text{ g} \cdot \text{kg}^{-1}$	10.32	0.22
	$0.3\text{ g} \cdot \text{kg}^{-1}$	9.85	0.22
	$1.1\text{ g} \cdot \text{kg}^{-1}$	11.07	0.21
	$4.4\text{ g} \cdot \text{kg}^{-1}$	11.69	0.24
	$28.2\text{ g} \cdot \text{kg}^{-1}$	11.04	0.23
Organic Matter	0%	13.71	0.22
	5%	11.11	0.22
	10%	11.54	0.22
	20%	11.79	0.25
	30%	12.44	0.24
Compaction	$0.9\text{ g} \cdot \text{cm}^{-3}$	7.74	0.23
	$1.0\text{ g} \cdot \text{cm}^{-3}$	10.60	0.20
	$1.1\text{ g} \cdot \text{cm}^{-3}$	10.60	0.20
	$1.3\text{ g} \cdot \text{cm}^{-3}$	14.07	0.26
	$1.5\text{ g} \cdot \text{cm}^{-3}$	13.07	0.24

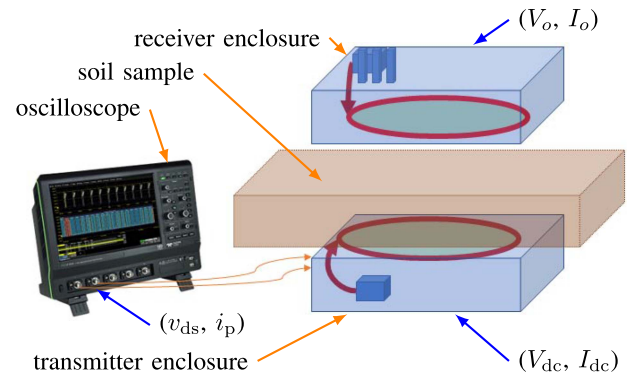


Fig. 10. Diagram of the experimental setup and the variables to acquire.

E. Experimental Setup

The experimental setup was assembled as shown in the photographs in Fig. 11. The transmitter enclosure was placed on a concrete floor (the transmit coil sits 5 mm in height under the lid on top of the enclosure) with two nonconductive enclosures on each side to support the soil sample under test. The receiver enclosure was placed on top of the soil sample enclosure in alignment with the transmitter enclosure. Between the receiver coil and the soil, there was a gap of 100 mm. The receiver coil sat 20 mm in height from the external bottom face of the enclosure, and the soil sample fills the enclosure up to 100 mm in height leaving an additional 80 mm of air.

The gap between the transmit coil and the soil was 20 mm, for a total distance from coil to coil of 200 mm, which corresponds to a coupling factor of 5.1% in air.

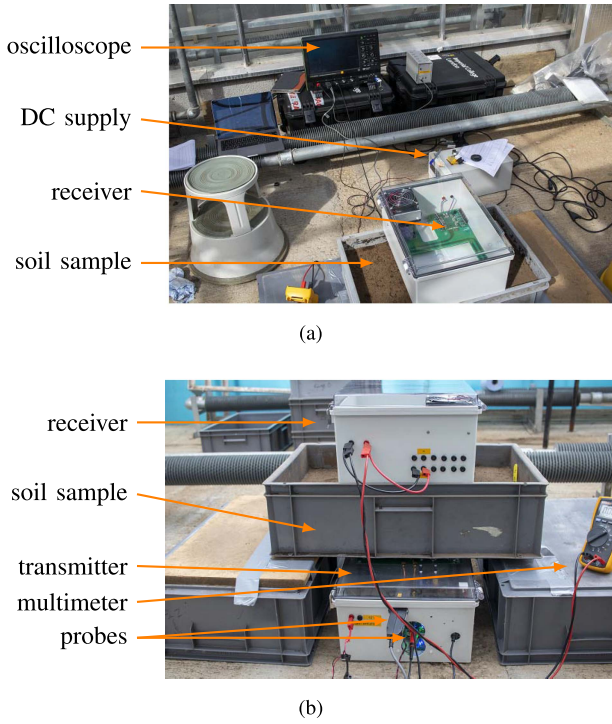


Fig. 11. Photographs of the experimental setup. (a) Top view. (b) Lateral view.

F. Experimental Results With the Soil Samples

IPT was performed and the variables V_{dc} , I_{dc} , V_o , R_o , v_{ds} , and i_p were recorded for the empty enclosure and the 19 soil samples, stepping the parameters of water content, salinity, organic matter, and compaction as detailed in Section IV-C. The temperature of the inverter board was monitored to ensure that changes in the temperature of the transistor would not affect the measurements. Also, the dc load resistance was verified at different temperatures to ensure consistency throughout the operating temperature range. The wireless power transfer results are summarized in the plots in Figs. 12–14. The results from the experiments where water was added in real time to the sample with a $4.4\text{-g} \cdot \text{kg}^{-1}$ proportion of NaCl and soil are summarized in Fig 15.

The end-to-end dc-to-dc efficiency measurements were conducted at maximum load, i.e., $R_o = 100 \Omega$. The end-to-end efficiency of the system without the presence of soil was measured at 53.4%. The power levels range from 11.3 to 19.4 W, and the coupling factor was measured at 5.1% for a coil separation of 200 mm without a soil sample. Having soil present decreased the end-to-end efficiency of the system with the exception of the sample with the highest compaction. This is due to the soil sample container walls being bent in the compaction process, therefore bringing the coils slightly closer together, which increased output power by 43% with respect to the experiment without soil, hence also increasing the efficiency. It is worth noting that this system configuration can achieve an end-to-end efficiency higher than 80% at couplings under 10% [18], [39] when the output power is much higher than the biasing power, which for this inverter, at 61.8-V input voltage, is 6.8 W.

In order to assess the causes for the drop in efficiency once the samples of soil were introduced, the reflected resistance and reactance are evaluated.

The reflected resistance was used to calculate the losses of the system without including the inverter by subtracting the output dc power from the output power of the transmit coil as

$$P_{\text{loss}} = \frac{R_{\text{eq}} |i_p|^2}{2} - V_o I_o \quad (6)$$

which can then be normalized with respect to the output power from the transmit coil as

$$P_{\text{loss-norm}} = 1 - \frac{2V_o I_o}{R_{\text{eq}} |i_p|^2}. \quad (7)$$

The plots of the normalized losses after the transmit coil suggest a consistent increase in the losses with respect to water content and salinity, and the plots show a less distinctive correlation with the variables of organic matter content and compaction.

In order to assess the detuning of the resonant circuits from the presence of the soil samples, which might also cause the efficiency to drop, the reflected reactance from the receiver and the soil was plotted in Fig. 14. These plots demonstrate the dependence of the reflected reactance to the load resistance in Class D rectifiers at 13.56 MHz first verified with this technique in [40], and how soil also consistently increases X_{eq} . Notwithstanding that, in the setup, the soil sample is closer to the transmitter, measurements were also conducted without a receiver in place to confirm that the reflected positive reactance in the experiments without a receiver is due to the soil directly reflecting a positive reactance and not the soil reflecting a negative reactance on the receiver, which consequently would reflect a positive reactance on to the transmitter. Interestingly, the plots suggest that higher water content slightly increases X_{eq} and salinity slightly decreases it.

G. Experimental Results With the Addition of Water in Real Time

Once the experiments with every soil sample were finalized, an additional experiment was conducted. Water was added to a sample with high salinity ($4.4\text{-g} \cdot \text{kg}^{-1}$ proportion of NaCl and soil, see Table IV), which was placed between the coils. The IPT system was switched ON periodically to take readings. A single dosage of 4 L of water was added at the surface of the sample once the two ends of the system were in place. The water was gradually absorbed by the soil. A thin polyester fiber for consistent water distribution at the surface was placed on top of the soil sample, and since the compaction of the soil was controlled as the samples were prepared, the water absorption is assumed uniform. At first, the pool of water sat on top of the sample, after 17 min (1020 s), the pool of water on top of the sample halved, and after 29 min (1740 s), the water was fully absorbed by the sample. With respect to the experiments in Section IV-F, this one has the benefit that the alignment of the boxes and the sample were unmodified while the variables could be measured in real time. Therefore, small discrepancies

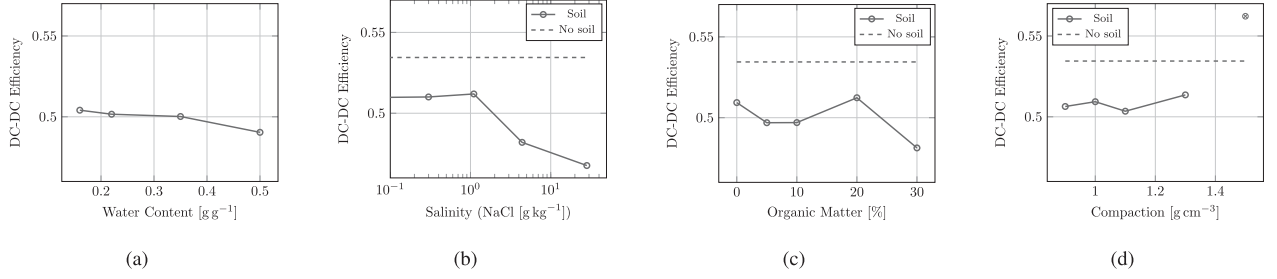


Fig. 12. End-to-end DC-DC efficiency measurements of HF-IPT through the samples of soil between the coils and an output dc load of $100\ \Omega$. Unrepresentative data points are marked as \otimes .

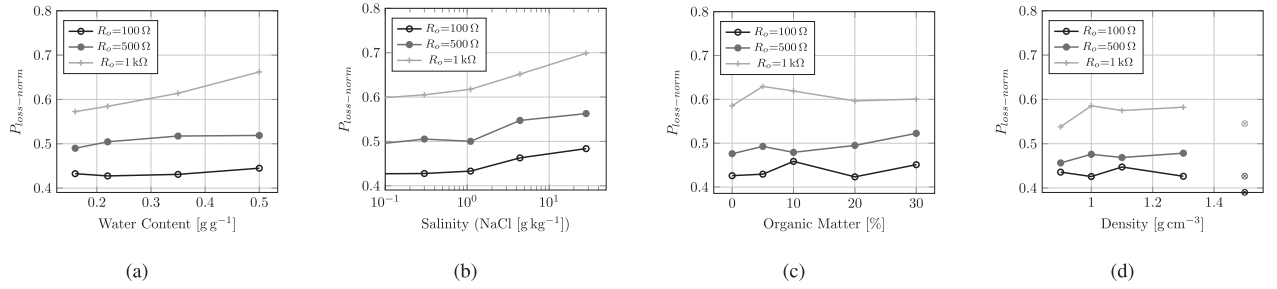


Fig. 13. Calculated normalized losses of HF-IPT through the samples of soil between the coils with three different DC loads. Unrepresentative data points are marked as \otimes .

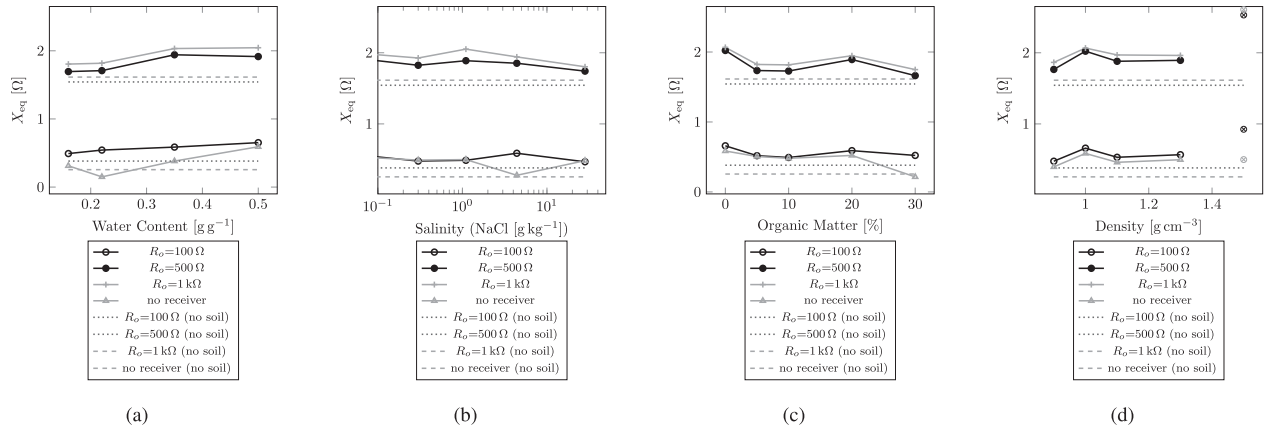


Fig. 14. Calculated reflected reactance from the receivers and the soil of HF-IPT through the samples of soil between the coils with three different DC loads, and without a receiver. Unrepresentative data points are marked as \otimes .

between the distance and alignment of the coils are not a factor of error in this experiment.

The absorption of water caused the end-to-end efficiency to drop from 25% to 18%, which corresponds to the losses increasing from 10.9 to 16.0 W. The normalized losses, calculated from (7), rose gradually from 0.55 to 0.74 throughout the experiments.

The behavior of the reflected reactance to the transmitter in this experiment is interesting, since compared to the initial reading without water, X_{eq} first rose as the water was added to the sample but then consistently decreased as the water

was absorbed by the soil with high salinity, making it more conductive. This is consistent with the observations of X_{eq} in Section IV-F, further supporting the observation that the water content and the salinity affect X_{eq} in opposing directions.

V. HF-IPT SYSTEM TO PERIODICALLY ENERGIZE AGRICULTURAL SOIL-SENSORS UNDER THE GROUND

Delivering power wirelessly to soil sensors under the ground in agricultural fields using HF-IPT was trialed with a 100-W, 13.56-MHz IPT system based on the combination of a Class EF

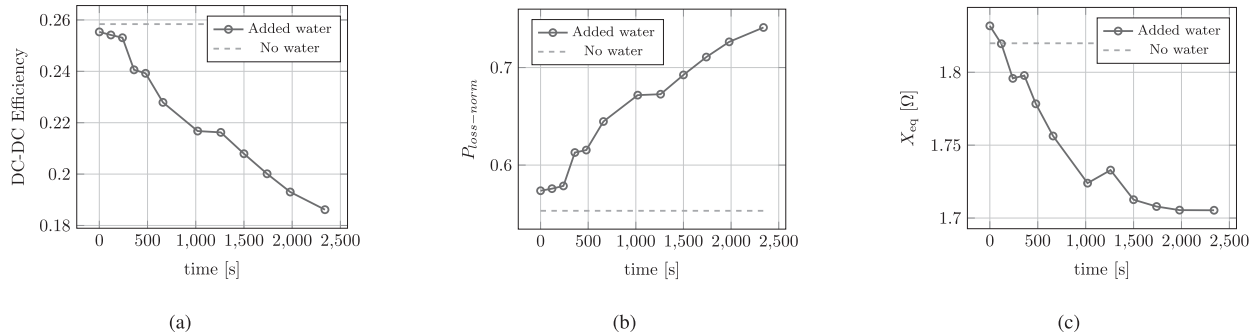


Fig. 15. End-to-end DC–DC efficiency measurements, normalized losses, and reflected reactance of HF-IPT through a sample of soil with high salinity between the coils, and the addition of 4 L of water, gradually wetting the soil.

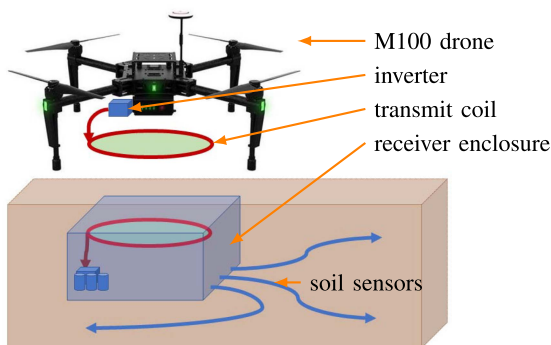


Fig. 16. Diagram of the setup for wireless charging of a sensor node.

inverter and a voltage tripler Class D rectifier. This is the same combination of circuits used in Section IV. The proposed application is illustrated in the diagram in Fig. 16, and the power delivery process is summarized in the block diagram in Fig. 17.

The setup proposes power delivery and the data gathering using a drone or a robot to reach the surface of the agricultural field where the sensor node is buried. Once the drone lands, it wirelessly charges a battery or a bank of supercapacitors under the ground while collecting the data from the sensors. It is important that the positioning accuracy capability of the drone is sufficient to align the coils with the precision required by the technology, and thus achieve the minimum coupling to transfer power effectively. In this demonstration, we used an M100 drone by DJI, and we buried an enclosure (length: 370 mm, width: 270 mm, height: 150 mm) with an IP67 rating containing an HF-IPT receiver, a bank of supercapacitors (10 F, 42 V), ultimately as the load, and other electronics for the soil sensors and monitoring. The bank of supercapacitors, as opposed to a bank of batteries, was proposed at the back-end of the system in order to perform fast charging in short missions, and then slowly charge the batteries of the soil-sensing system at low voltage with a dc–dc converter from the energy in the supercapacitors. The trial features the enclosure at 200 mm in depth from the lid of the enclosure (top face) to the soil surface of the field. The coupling range of the system is 3% to 5%, which in this application is achieved with a lateral alignment tolerance of roughly 100 mm

in any direction, and irrespective of the angular alignment, i.e., the drone can land within 100 mm of concentric alignment of the coils, facing in any direction to achieve effective wireless power transfer.

The work reported in this article focuses on power delivery through the soil using HF-IPT. The developments of other aspects of this setup can be found in [27], [41], and [42].

A. Power Electronic Stages for Wireless Power Transfer

Power is processed from end to end (see Fig. 17) as follows: energy from the battery of the drone (a TB47D battery by DJI), which has a capacity of 4500 mAh and a nominal voltage of 22.2 V, feeds an in-house boost converter, which provides the inverter of the HF-IPT system with an input voltage (V_{dc}) of 95 V and a maximum input current of 1 A. The inverter drives the transmit coil with a coil current (i_p) amplitude of 5.7 A to induce a voltage (\mathcal{E}_{p-s}) on the receiver coil, which is then rectified to V_o using a voltage multiplier rectifier. From V_o , we power an off-the-shelf converter to charge a bank of supercapacitors with constant current (CC) at a voltage lower than 42 V, and at constant voltage (CV) once that threshold is reached. The efficiency measurements in this section are measured from the input voltage before the boost converter that drives the HF-IPT inverter to the supercapacitors, after the HF-IPT rectifier.

B. Design of the HF-IPT System

The circuits implemented in the demonstrator are shown in the photographs of Figs. 18 and 19. The transmitter features a single-turn 10-mm diameter 0.9-mm wall-thickness copper-pipe circular coil with a 200-mm radius [see Fig. 18(a)], designed with this shape and materials to achieve a large gap and high efficiency without heavily affecting the propeller thrust.

The inverter [topology in Fig. 3 and photograph in Fig. 18(b)] implements the same reference load-independent design as the one in Section IV-B. The differences (Design 2 in Table II) are that the transmit coil of this system has a different construction but the same inductance at 13.56 MHz as the PCB coil in Section IV-B, and since this system operates the inverter at a higher input voltage (95 V instead of 61.8 V), the tuning required

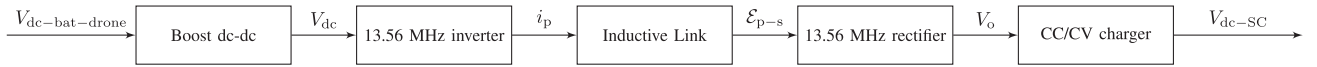


Fig. 17. Drone to soil sensor enclosure power-delivery block diagram.

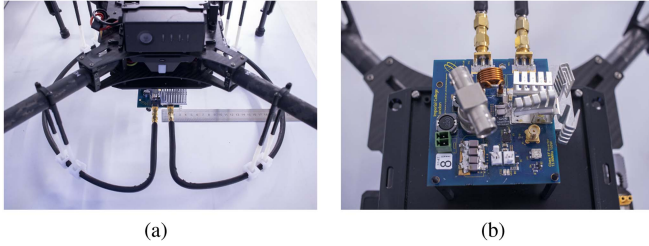


Fig. 18. Photographs of the HF-IPT transmitter on the Matrice 100 drone. (a) Transmit coil. (b) HF-IPT inverter board.

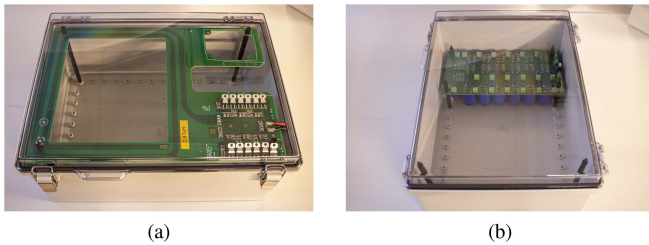


Fig. 19. Photographs of the receiver enclosure. (a) Coil and rectifier PCB. (b) Bank of supercapacitors.

adding 10 pF to C_1 (see Fig. 3) due to the C_{OSS} of the transistor being lower at higher voltages.

The receiver [see Fig. 19(a)] features the rectifier design detailed in Table III, but instead of feeding a dc test load from the output of the rectifier as in Section IV, this system feeds an off-the-shelf 42-V lithium polymer battery charger by KDF, which charges an in-house bank of supercapacitors [see Fig. 19(b)], comprised of 20 SSC-Series 200 F supercapacitors by AVX in series.

The HF-IPT system was designed for a coil separation from 250 to 300 mm in air, where the expected coupling range (3% to 5%) is achieved with a lateral alignment tolerance of one receiver coil radius in any direction, and independent on the angular alignment, i.e., once the center of the coils are aligned, the drone can be facing any direction without a significant impact on coupling. At a coil distance of 250 mm and concentric alignment, the coupling was measured at 4.9%, and with a 100-mm lateral misalignment at 3.1%.

C. Setup in the Laboratory

The photograph of the setup in the laboratory in Fig. 20 shows the HF-IPT system in place, operating with a coil-to-coil gap of 290 mm.

First, a series of experiments were conducted on the charger and the bank of supercapacitors to characterize it and define it as the load, which is coupled to the HF-IPT rectifier. The input

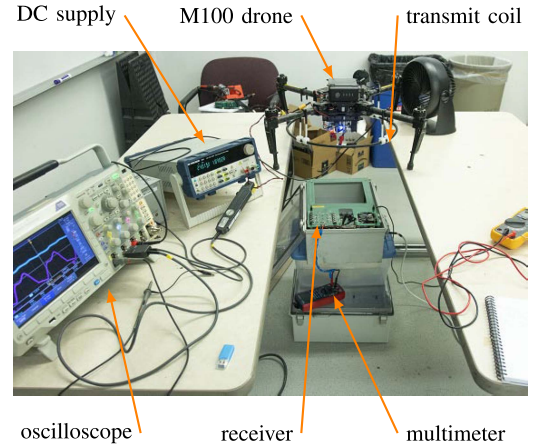


Fig. 20. Test setup in the laboratory.

TABLE V
CHARACTERISTICS OF THE BANK OF SUPERCAPACITORS WITH ITS CHARGER

Parameter	V_{s-caps} and I_{s-caps}	Value
Energy capacity	42 V	8.8 kJ (100 %)
Energy capacity	20 V	2.0 kJ (22.7 %)
Charging power	42 V, 350 mA	14.7 W (100 %)
Charging power	20 V, 350 mA	7.0 W (47.6 %)
Charging time	20–42 V, 350 mA	660 s
Charging power	42 V, 825 mA	34.7 W (100 %)
Charging power	20 V, 825 mA	16.5 W (47.6 %)
Charging time	20–42 V, 825 mA	300 s

voltage range of the charger, which is also the output voltage of the HF-IPT rectifier (V_o), is 95–240 V. The output current of the charger when it operates in CC was first set at 350 mA and then at 825 mA. When the output voltage of the charger (the voltage of the bank of supercapacitors) drops under 20 V, instead of charging at CC, the off-the-shelf charger outputs current pulses. This undervoltage protection, typical in lithium polymer battery charging, was convenient for the trial to protect the transmitter against possible faults in the receiver, which should be considered given the harsh nature of its environment. This feature, however, results in slower charging from 0 to 20 V. In the experiments, the performance of the system is evaluated when the charger operates in CC, i.e., with the supercapacitors voltage from 20 to 42 V. The specifications and the charging profile of the supercapacitors are summarized in Table V. Fig. 21(a) and (b) shows the voltage and current of the supercapacitors as they charge from 20 to 42 V with an average current of 350 mA.

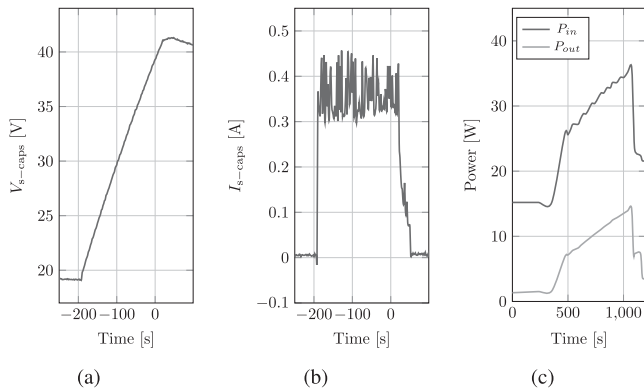


Fig. 21. Plots of the experiments charging the bank of supercapacitors. (a) Supercapacitors voltage. (b) Supercapacitors current. (c) Input power of the HF-IPT system and output power to the bank of supercapacitors.

TABLE VI
SUMMARY OF THE EXPERIMENTAL RESULTS OF WIRELESS POWER FROM THE DRONE TO THE SUPERCAPACITORS

Medium	Parameter	V_{s-caps} and I_{s-caps}	Value	Efficiency
Air	Input power	20 V, 350 mA	25.6 W	28 %
	Input power	42 V, 350 mA	36.8 W	40 %
	Input energy	20–42 V, 350 mA	20.06 kJ	34 %
Air	Input power	20 V, 825 mA	38.2 W	43 %
	Input power	42 V, 825 mA	62.9 W	55 %
	Input energy	20–42 V, 825 mA	15.2 kJ	45 %
Soil	Input power	20 V, 825 mA	60.0 W	28 %
	Input power	42 V, 825 mA	92.9 W	37 %
	Input energy	20–42 V, 825 mA	22.9 kJ	30 %

Fig. 21(c) shows the input power of the HF-IPT system and the input power of the supercapacitors as they charge from 20 to 42 V with an average current of 350 mA. The experiments were conducted using the setup shown in Fig. 20, where the coupling factor is 4.9% and the output voltage of the rectifier is approximately 180 V. As the lateral misalignment is increased, the output voltage of the rectifier drops. If this is reduced to a voltage lower than 90 V, the undervoltage protection of the supercapacitor charger is triggered and the transfer of power is interrupted. These experiments were repeated stepping the lateral misalignment between the coils up until the output voltage of the rectifier was 120 V, considering a safety margin. The charging of the supercapacitors was performed in the same time lapse (as this depends on the current set by the supercapacitors charger, and the profile of the input power of the system was very similar: The inverter drives the coil with a constant i_p , so its performance is not expected to change, the rectifier becomes slightly less efficient as the induced voltage in the receive coil is reduced, but the efficiency of the supercapacitor charger increases as the difference between its input voltage (the output voltage of the rectifier) and output voltage (the voltage of the supercapacitors) increases. Table VI provides a summary of the results of charging the supercapacitors at 350



Fig. 22. Photograph of the preliminary test setups in the agricultural field.

and 825 mA. The experiments in the laboratory and in the field were conducted employing a bench power supply at 22 V instead of using the drone's battery, in the laboratory for monitoring and safety, and in the field due to low ambient temperatures, which caused the drone's battery to be disabled.

D. Results From the Six-Week Trial in the Field

The laboratory setup was replicated in the field. The experiments were conducted near a dormant carnation flower (*Dianthus caryophyllus*) testbed at Utah State University Botanical Center in Davis County, Utah, USA, between February 10, 2022, and March 22, 2022. The bulk density of the soil above the receiver station was $1.01 \text{ g} \cdot \text{cm}^{-3}$ (measured by oven-drying at 105°C and weighing a 937.8-cm^3 core sample). This indicates that soil above the receiver had compaction comparable to the second lowest from the samples in Section IV. The water content of the sample was measured at $23.2 \text{ g} \cdot \text{g}^{-1}$; however, in the field, this would change with precipitation. The electric conductivity was measured at $0.09 \text{ dS} \cdot \text{m}^{-1}$, and the pore water electric conductivity was measured at $0.87 \text{ dS} \cdot \text{m}^{-1}$, suggesting that the sample has a salinity within the range of the second and third samples, $0.3 \text{ g} \cdot \text{kg}^{-1}$ and $1.1 \text{ g} \cdot \text{kg}^{-1}$ of added NaCl, from the samples in Section IV.

First, the system was tested without soil covering the receiver enclosure (see Fig. 22) to allow the circuits at the receiver to be probed. It was not necessary to adjust the tuning of the inverter or the rectifier. However, a slight increase in the input power of the system and the shape of the drain-voltage waveforms of the inverter suggest an increasing total load to the transmit coil and no significant detuning in comparison to the experiments in the laboratory. Moreover, the receiver in the soil reflected a higher resistance and roughly the same reactance as in the laboratory. Once the correct operation of both ends of the HF-IPT system was verified in location, the receiver enclosure lid was closed and the enclosure was covered with soil. The depth between the surface and the top face of the enclosure was measured at 200 mm. In order to verify the operation of the HF-IPT system, a circuit to read the voltage of the bank of supercapacitors was developed using an off-the-shelf Bluetooth transmitter inside the receiver enclosure. Fig. 23 shows a photograph of the wireless power demonstration from a transmitter mounted on a drone to a receiver surrounded and covered with soil in an agricultural



Fig. 23. Photograph of an M100 drone performing HF-IPT through the soil in a trial in an agricultural field.

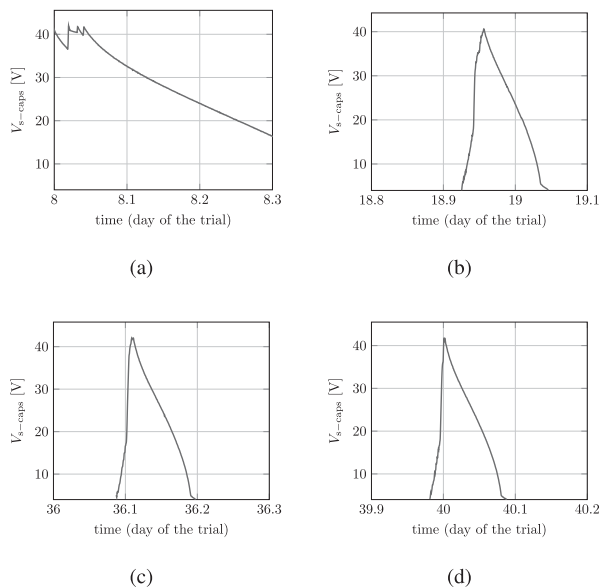


Fig. 24. Voltage of the supercapacitors during the four wireless power transfer experiments in the trial.

field. The results of the experiment are summarized in Table VI. As expected, the efficiency is lower than that achieved in the laboratory, due to additional loading from the soil, which is consistent with the results investigated in Section IV with this composition of the soil. Equally, no significant changes in H_1 were detected from the experimental waveforms, suggesting that the change in the reflected reactance is low, according to (5).

The bank of supercapacitors was designed to be slowly discharged by a battery charger, which feeds the main power supply of the sensor node, also containing a small battery.

The operation of the sensor node was trialed for six weeks, and wireless charging was performed four times, in addition to the experiments conducted when the enclosure was first put in place. The input power measured in the first experiment was consistent with the subsequent wireless charging experiments. The voltage of the bank of supercapacitors was recorded for the entire duration of the trial. Fig. 24 shows the voltage in the supercapacitors during the four occasions where wireless power was performed.

The first charge, during the eighth day of the trial [see Fig. 24(a)] focuses on the slow discharge of the supercapacitors

due to the battery of the sensor node being close to fully charged (probably charging at CV and not CC). It should be noted that the plots in Fig. 24 are at the same scale in both axes. The second charge [see Fig. 24(b)] shows disruptions at peak voltage. This is due to the drone not being placed within the wireless charging range (the coupling was slightly lower than the minimum, determined in the laboratory at 3%), which as the load increases (at CC when the voltage of the bank of supercapacitors increases so does the load), the input voltage of the charger diminished until the undervoltage protection was triggered. Once the drone was placed correctly on top of where the receiver enclosure was buried, the supercapacitors were fully charged.

After 40 days, the receiver was dug out and the data from the experiment, including the voltage of the supercapacitors, were gathered.

VI. CONCLUSION

This article investigates the viability of employing HF-IPT in agricultural applications where it is unpractical or impossible to have wired links.

The differences in the performance of the system with respect to the physical composition of the soil (water content, salinity, organic matter, and compaction) were investigated. The results in Section IV demonstrate that the presence of soil slightly affects the tuning of an IPT system at 13.56 MHz by reflecting a small positive reactance to the coils, and with the exception of the sample combining high water content and high salinity, the results are encouraging, as they also had a low impact on the end-to-end efficiency. These experiments, therefore, support the technical viability of using IPT at 13.56 MHz to wirelessly energize loads beneath the surface in agricultural applications.

The system demonstrator in Section V exemplifies an HF-IPT system delivering power under the ground at considerable depths (200 mm in this case), to enable power for sensors under the ground and, therefore, contribute to automation and optimization in agriculture.

REFERENCES

- [1] S. Y. Hui, "Planar wireless charging technology for portable electronic products and Qi," *Proc. IEEE*, vol. 101, no. 6, pp. 1290–1301, Jun. 2013.
- [2] S. Li and C. C. Mi, "Wireless power transfer for electric vehicle applications," *IEEE Trans. Emerg. Sel. Topics Power Electron.*, vol. 3, no. 1, pp. 4–17, Mar. 2015.
- [3] G. Covic and J. T. Boys, "Modern trends in inductive power transfer for transportation applications," *IEEE Trans. Emerg. Sel. Topics Power Electron.*, vol. 1, no. 1, pp. 28–41, Mar. 2013.
- [4] K. V. Schuylenbergh and R. Puers, *Inductive Powering: Basic Theory and Application to Biomedical Systems*. Berlin, Germany: Springer, 2009.
- [5] B. Lenaerts and R. Puers, *Omnidirectional Inductive Powering for Biomedical Implants*. Berlin, Germany: Springer, 2009.
- [6] S. Kim, J. S. Ho, and A. S. Y. Poon, "Wireless power transfer to miniature implants: Transmitter optimization," *IEEE Trans. Antennas Propag.*, vol. 60, no. 10, pp. 4838–4845, Oct. 2012.
- [7] T. Campi, S. Cruciani, F. Palandrani, V. De Santis, A. Hirata, and M. Feliziani, "Wireless power transfer charging system for AIMDs and pacemakers," *IEEE Trans. Microwave Theory Techn.*, vol. 64, no. 2, pp. 633–642, Feb. 2016.
- [8] D. Floreano and R. J. Wood, "Science, technology and the future of small autonomous drones," *Nature*, vol. 521, no. 7553, pp. 460–466, 2015.

- [9] K. Zhang et al., "Aerial additive manufacturing with multiple autonomous robots," *Nature*, vol. 609, no. 7928, pp. 709–717, 2022.
- [10] P. D. Mitcheson et al., "Energy-autonomous sensing systems using drones," in *Proc. IEEE SENSORS*, 2017, pp. 1–3.
- [11] I. F. Akyildiz and E. P. Stuntebeck, "Wireless underground sensor networks: Research challenges," *Ad Hoc Netw.*, vol. 4, no. 6, pp. 669–686, 2006.
- [12] E. Vories and K. Sudduth, "Determining sensor-based field capacity for irrigation scheduling," *Agricultural Water Manage.*, vol. 250, 2021, Art. no. 106860.
- [13] Y. Su, X. Liu, and S. R. Hui, "Mutual inductance calculation of movable planar coils on parallel surfaces," *IEEE Trans. Power Electron.*, vol. 24, no. 4, pp. 1115–1123, Apr. 2009.
- [14] C. R. Sullivan, B. A. Reese, A. L. Stein, and P. A. Kyaw, "On size and magnetics: Why small efficient power inductors are rare," in *Proc. Int. Symp. 3D Power Electron. Integration Manuf.*, 2016, pp. 1–23.
- [15] A. Kurs, A. Karalis, R. Moffatt, J. D. Joannopoulos, P. Fisher, and M. Soljačić, "Wireless power transfer via strongly coupled magnetic resonances," *Science*, vol. 317, no. 5834, pp. 83–86, 2007.
- [16] M. Pinuela, D. C. Yates, S. Lucyszyn, and P. D. Mitcheson, "Maximizing DC-to-load efficiency for inductive power transfer," *IEEE Trans. Power Electron.*, vol. 28, no. 5, pp. 2437–2447, May 2013.
- [17] J. M. Arteaga, S. Aldhafer, G. Kkelis, C. Kwan, D. C. Yates, and P. D. Mitcheson, "Dynamic capabilities of multi-MHz inductive power transfer systems demonstrated with batteryless drones," *IEEE Trans. Power Electron.*, vol. 34, no. 6, pp. 5093–5104, Jun. 2019.
- [18] G. Zulauf and J. M. R. Davila, "Single-turn air-core coils for high-frequency inductive wireless power transfer," *IEEE Trans. Power Electron.*, vol. 35, no. 3, pp. 2917–2932, Mar. 2020.
- [19] J. Choi, D. Tsukiyama, Y. Tsuruda, and J. Rivas, "13.56 MHz 1.3 kW resonant converter with GaN FET for wireless power transfer," in *Proc. IEEE Wireless Power Transfer Conf.*, 2015, pp. 1–4.
- [20] D. J. Perreault et al., "Opportunities and challenges in very high frequency power conversion," in *Proc. IEEE 24th Annu. Appl. Power Electron. Conf. Expo.*, 2009, pp. 1–14.
- [21] F. Lu, H. Zhang, and C. Mi, "A review on the recent development of capacitive wireless power transfer technology," *Energies*, vol. 10, no. 11, 2017, Art. no. 1752.
- [22] L. J. Zou, Q. Zhu, C. W. V. Neste, and A. P. Hu, "Modeling single-wire capacitive power transfer system with strong coupling to ground," *IEEE Trans. Emerg. Sel. Topics Power Electron.*, vol. 9, no. 2, pp. 2295–2302, Apr. 2021.
- [23] B. T. Nieman et al., "Through the soil long range wireless power transfer for agricultural IoT networks," *IEEE Trans. Ind. Electron.*, vol. 71, no. 2, pp. 2090–2099, Feb. 2024, doi: [10.1109/TIE.2023.3250743](https://doi.org/10.1109/TIE.2023.3250743).
- [24] B. Lin and A. B. Cerato, "Electromagnetic properties of natural expansive soils under one-dimensional deformation," *Acta Geotechnica*, vol. 8, no. 4, pp. 381–393, 2013.
- [25] K. A. Klein and J. C. Santamarina, "Electrical conductivity in soils: Underlying phenomena," *J. Environ. Eng. Geophys.*, vol. 8, no. 4, pp. 263–273, 2003.
- [26] J. M. Arteaga, P. D. Mitcheson, and E. M. Yeatman, "Development of a fast-charging platform for buried sensors using high frequency IPT for agricultural applications," in *Proc. IEEE Appl. Power Electron. Conf. Expo.*, 2022, pp. 1116–1121.
- [27] J. Sanchez et al., "Integration of a high frequency inductive power transfer system to energize agricultural sensors through soil," in *Proc. Wireless Power Week*, 2022, pp. 366–371.
- [28] N. O. Sokal and A. D. Sokal, "Class E—A new class of high-efficiency tuned single-ended switching power amplifiers," *IEEE J. Solid-State Circuits*, vol. JSSC-10, no. 3, pp. 168–176, Jun. 1975.
- [29] R. C. N. Pilawa-Podgurski, A. D. Sagneri, J. M. Rivas, D. I. Anderson, and D. J. Perreault, "Very-high-frequency resonant boost converters," *IEEE Trans. Power Electron.*, vol. 24, no. 6, pp. 1654–1665, Jun. 2009.
- [30] Z. Kaczmarczyk, "High-efficiency class E, EF_2 , and E/F_3 inverters," *IEEE Trans. Ind. Electron.*, vol. 53, no. 5, pp. 1584–1593, Oct. 2006.
- [31] L. Gu, G. Zulauf, Z. Zhang, S. Chakraborty, and J. Rivas-Davila, "Push-pull class ϕ_2 RF power amplifier," *IEEE Trans. Power Electron.*, vol. 35, no. 10, pp. 10515–10531, Oct. 2020.
- [32] S. Aldhafer, D. C. Yates, and P. D. Mitcheson, "Load-independent class E/EF inverters and rectifiers for MHz-switching applications," *IEEE Trans. Power Electron.*, vol. 33, no. 10, pp. 8270–8287, Oct. 2018.
- [33] I. Nikiforidis, J. M. Arteaga, C. H. Kwan, N. Pucci, D. C. Yates, and P. D. Mitcheson, "Generalized multistage modeling and tuning algorithm for class EF and class ϕ inverters to eliminate iterative retuning," *IEEE Trans. Power Electron.*, vol. 37, no. 10, pp. 12877–12900, Oct. 2022.
- [34] J. M. Arteaga, N. Pucci, L. Lan, and P. D. Mitcheson, "Load characterization in high-frequency IPT systems using class EF switching waveforms," *IEEE Trans. Power Electron.*, vol. 36, no. 10, pp. 11036–11044, Oct. 2021.
- [35] N. Pucci, J. M. Arteaga, C. H. Kwan, D. C. Yates, and P. D. Mitcheson, "Induced voltage estimation from class EF switching harmonics in HF-IPT systems," *IEEE Trans. Power Electron.*, vol. 37, no. 4, pp. 4903–4916, Apr. 2022.
- [36] N. Pucci, J. M. Arteaga, and P. D. Mitcheson, "Dynamic receiver characterization in HF-IPT systems," in *Proc. Wireless Power Week*, 2022, pp. 308–312.
- [37] J. M. Arteaga, L. Lan, S. Aldhafer, G. Kkelis, D. C. Yates, and P. D. Mitcheson, "A multi-MHz IPT-link developed for load characterisation at highly variable coupling factor," in *Proc. IEEE Wireless Power Transfer Conf.*, 2018, pp. 1–4.
- [38] M. M. Weiner, "Analysis of Cockcroft-Walton voltage multipliers with an arbitrary number of stages," *Rev. Sci. Instruments*, vol. 40, no. 2, pp. 330–333, 1969.
- [39] J. M. Arteaga, S. Aldhafer, G. Kkelis, D. C. Yates, and P. D. Mitcheson, "Multi-MHz IPT systems for variable coupling," *IEEE Trans. Power Electron.*, vol. 33, no. 9, pp. 7744–7758, Sep. 2018.
- [40] J. M. Arteaga, L. Lan, C. H. Kwan, D. C. Yates, and P. D. Mitcheson, "Characterisation of high frequency inductive power transfer receivers using pattern recognition on the transmit side waveforms," in *Proc. IEEE Appl. Power Electron. Conf. Expo.*, 2020, pp. 825–831.
- [41] J. Sanchez et al., "Misalignment parameterization of a 13.56 MHz inductive power transfer system for in-situ soil sensing," in *Proc. 21st Int. Conf. Micro Nanotechnol. Power Gener. Energy Convers. Appl.*, 2022, pp. 278–281.
- [42] T. Polonelli, M. Magno, V. Niculescu, L. Benini, and D. Boyle, "An open platform for efficient drone-to-sensor wireless ranging and data harvesting," *Sustain. Comput. Inform. Syst.*, vol. 35, 2022, Art. no. 100734.



Juan M. Arteaga received the B.Sc. and Licentiate (Hons.) degrees in electrical engineering from the University of Costa Rica, San Pedro, Costa Rica, in 2008 and 2010, respectively, the M.Sc. degree in micro and nanoelectronics from the Autonomous University of Barcelona, Bellaterra, Spain, in 2011, and the Ph.D. degree in electrical and electronic engineering from Imperial College London, London, U.K., in 2020.

He is currently a Research and Development Power Electronics Engineer with NewOrbit Space, Ltd., Reading, U.K., focusing on air-breathing electric propulsion to enable operation at very low Earth orbit. His research interests include power electronics, high-frequency resonant power converters, plasma propulsion engines, and wireless power transfer.

Dr. Arteaga was the recipient of the 2019 IEEE Transactions on Power Electronics Second Prize Paper Award and the Eryl Cadwallader Davies Prize for his Ph.D. dissertation.



John Sanchez received the M.S. degree in mechanical engineering from the New Mexico Institute of Mining and Technology, Socorro, NM, USA, in 2020. He is currently working toward the Ph.D. degree in mechanical engineering with The University of Utah, Salt Lake City, UT, USA.

His research interests include robotics, embedded systems, and wireless power transfer.



Faraj Elsakloul received the B.Sc. degree in agricultural science, specializing in soil and water, from the University of Sirte, Sirte, Libya, in 2009, and the M.Sc. degree in soil science in 2015 from the University of Aberdeen, Aberdeen, U.K., where he is currently working toward the Ph.D. degree in soil science particularly soil physics.

His research interest focuses on investigating the interaction between plants and saline-sodic soil.



Maria Marin received the B.Sc. degree in biological sciences and the M.Sc. degree in environmental biology from the University of Trieste, Trieste, Italy, in 2011 and 2014, respectively, and the Ph.D. degree in Earth and environmental sciences, supported by the Marie Skłodowska-Curie Actions, from the University of Pavia, Pavia, Italy, in 2017.

She is currently a Research Fellow with Soil Biophysics Group, School of Biological Sciences, University of Aberdeen, Aberdeen, U.K. Her research interests include plant and soil interactions and plant

ecophysiology in the context of agricultural sustainability.



Cody Zesiger received the B.S. degree in zoology from Weber State University, Ogden, UT, USA, in 2016, and the M.A. degree in science education from Western Governors University, Millcreek, UT, in 2018.

He is currently an Extension Assistant Professor in agriculture and natural resources with Utah State University, Logan, UT. His research interests include forages, row crop production, production horticulture, and weed science.



Nunzio Pucci (Member, IEEE) received the M.Eng. and Ph.D. degrees in electrical and electronic engineering from Imperial College London, London, U.K., in 2019 and 2023, respectively.

He is currently with Imperial College London, where he is currently working on high-frequency wireless power transfer. His research interests include power electronics, resonant converters, wireless power transfer, and custom instrumentation.

Dr. Pucci is the recipient of three conference prizes, including the WoW 2021 IEEE Workshop on Emerging

Technologies: Wireless Power Best Paper Prize.



Gareth J. Norton received the B.Sc. and Ph.D. degrees in molecular biology from the University of Hertfordshire, Hatfield, U.K., in 2001 and 2005, respectively.

He is currently a Reader with the University of Aberdeen, Aberdeen, U.K. His research explores plant environment interactions. His current research interest includes integrating elemental concentrations within plants with genetic mapping, genomics, and transcriptomics, with the aim of identifying genes and mechanisms responsible for the accumulation of elements in plants.



Darrin J. Young (Senior Member, IEEE) received the B.S., M.S., and Ph.D. degrees from the Department of Electrical Engineering and Computer Sciences, University of California at Berkeley, Berkeley, CA, USA, in 1991, 1993, and 1999, respectively.

He joined the Department of Electrical Engineering and Computer Science, Case Western Reserve University, in 1999, as an Assistant Professor. In 2009, he joined Electrical and Computer Engineering Department, The University of Utah, as a USTAR Associate Professor. He has authored or coauthored many technical papers in high-impact journals and conferences. His research interests focus on microelectromechanical systems design and fabrication, integrated electronic interface circuits design, wireless power transfer, and microsystem packaging technology for a wide range of applications, including wireless sensing, implantable and wearable biomedical sensing, RF communication, industrial sensing, personal navigation, and environmental monitoring.

Dr. Young was a Technical Program Committee member and a Session Chair for a number of reputable international conferences. He was an Associate Editor for the IEEE JOURNAL OF SOLID-STATE CIRCUITS, the Chair of the IEEE Electron Devices Society MEMS Committee, and a member of the IEEE Sensors Council. He is currently an Editor of the IEEE TRANSACTIONS ON ELECTRON DEVICES.



David E. Boyle (Member, IEEE) received the B.Eng. degree in computer engineering and the Ph.D. degree in computer and electronic engineering from the University of Limerick, Limerick, Ireland, in 2005 and 2009, respectively.

He is currently an Associate Professor (Senior Lecturer) with the Dyson School of Design Engineering, Imperial College London, London, U.K. His research interests include the design of secure, private, and trustworthy cyber-physical systems.



Eric M. Yeatman (Fellow, IEEE) received the B.S. degree in physics from Dalhousie University, Halifax, NS, Canada, in 1983, the B.Eng. degree in engineering physics from Technical University of Nova Scotia, Halifax, in 1985, the M.S. degree in physics from Dalhousie University, in 1986, and the Ph.D. degree from Imperial College London, London, U.K., in 1989.

He is currently a Professor in microengineering and the Head of Electrical and Electronic Engineering Department, Imperial College London. His research

interests include mechanical and optical MEMS, energy harvesting for wireless devices, sensor systems, and microrobotics.

Dr. Yeatman is a Fellow and the Silver Medalist of the Royal Academy of Engineering, and was a cofounder and the Director of Microsaic Systems, which develops and markets miniature mass spectrometers for portable chemical analysis.



Paul D. Hallett received the B.Sc. degree in agricultural sciences, specializing in soil science, from the University of Guelph, Guelph, ON, Canada, in 1992, and the Ph.D. degree in chemical engineering from the University of Birmingham, Birmingham, U.K., in 1996.

He is currently a Professor in soil physics with the University of Aberdeen, Aberdeen, U.K. His research explores solutions to food and environmental security, mainly focussed on the interactions between plants, microorganisms, and the physical behavior of soil.

Prof. Hallett is the President-Elect of the British Society of Soil Science.



Shad Roundy (Member, IEEE) received the M.S. and Ph.D. degrees in mechanical engineering from the University of California, Berkeley, Berkeley, CA, USA, in 2000 and 2003, respectively.

In 2012, he joined the faculty with The University of Utah, Salt Lake City, UT, USA, where he is currently an Associate Professor with the Department of Mechanical Engineering. From 2005 to 2012, he was with the MEMS industry developing tire pressure sensors, accelerometers, gyroscopes, and energy harvesters. From 2003 to 2005, he was a Lecturer with

Australian National University. His research interests include energy harvesting, wireless power transfer, and more generally MEMS sensors and actuators.

Dr. Roundy is a Fellow of the American Society of Mechanical Engineers.



Paul D. Mitcheson (Senior Member, IEEE) received the M.Eng. degree in electrical and electronic engineering and the Ph.D. degree in micropower-motion-based energy harvesting for wireless sensor networks from Imperial College London, London, U.K., in 2001 and 2005, respectively.

He is currently a Professor in electrical energy conversion with Control and Power Research Group, Electrical and Electronic Engineering Department, Imperial College London. His research has been supported by the European Commission, Engineering and Physical Sciences Research Council, and several companies. His research interests include energy harvesting, power electronics, and wireless power transfer to provide power to applications in circumstances where batteries and cables are not suitable.

Prof. Mitcheson is a Fellow of the Higher Education Academy and was on the executive committee of the U.K. Power Electronics Centre. He was the General Cochair of IEEE Wireless Power Week in 2019, London, U.K.